2019

Vibrational Characterization of Granulosa Cells From Patients Affected by Unilaterial Ovarian Endometriosis: New Insights From Infrared and Raman Microspectroscopy

Valentina Notarstefano
Universita Politecnica delle Marche, Italy

Giorgia Gioacchini
Universita Politecnica delle Marche, Italy

Hugh J. Byrne
Technological University Dublin, hugh.byrne@tudublin.ie

Carlotta Zaca
9.Baby Centre for Reproductive Heatlh, Bologna, Italy

Eleni Seren
Baby Center for Reproductive Health, Bologna, Italy

Follow this and additional works at: https://arrow.tudublin.ie/nanolart

Part of the Chemicals and Drugs Commons, and the Medical Sciences Commons

See next page for additional authors

Recommended Citation

Authors

Valentina Notarstefano, Giorgia Gioacchini, Hugh J. Byrne, Carlotta Zaca, Eleni Sereni, Lisa Vaccari, Andrea Borini, and Oliana Carnevali

Vibrational characterization of Granulosa Cells from patients affected by Unilateral Ovarian Endometriosis: new insights from infrared and Raman microspectroscopy

Valentina Notarstefano[a†], Giorgia Gioacchini[a†], Hugh J. Byrne[b], Carlotta Zacà[c],
Elena Sereni[c], Lisa Vaccari[d], Andrea Borini[c], Oliana Carnevali[a],
Elisabetta Giorgini[a*]

[a]Dipartimento di Scienze della Vita e dell'Ambiente, Università Politecnica delle Marche, via Brecce Bianche, 60131 Ancona, Italy
[b]FOCAS Research Institute, Dublin Institute of Technology, Kevin Street, Dublin 2, Ireland
[c]9.Baby Center for Reproductive Health, via Dante 15, 40125 Bologna, Italy
[d]SISSI Beamline, Elettra-Sincrotrone Trieste, S.C.p.A., S.S. 14 – Km 163.5, 34149 Basovizza, Trieste, Italy

† These authors equally contributed to this work

*Corresponding author.
E-mail address: e.giorgini@univpm.it (E. Giorgini)

ABSTRACT

_____

Endometriosis is a chronic gynaecological disease characterised by the presence of endometrial cells in extra-uterine regions. One of the main factors impacting on the fertility of women affected by endometriosis is the poor oocyte quality. Granulosa Cells (GCs) regulate oocyte development and maintain the appropriate microenvironment for the acquisition of its competence; hence, the dysregulation of these functions in GCs can lead to severe cellular damages also in oocytes. In this study, luteinized GCs samples were separately collected from both ovaries of women affected by Unilateral Ovarian Endometriosis and analyzed by infrared and Raman microspectroscopy. The spectral data were compared with those of GCs from women with diagnosis of tubal, idiopathic or male infertility (taken as control group). The coupling of these two spectroscopic techniques shed new light on the alteration induced by this pathology on GCs metabolism and biochemical composition. In fact, the study revealed in GCs from both ovaries of women affected by unilateral ovarian endometriosis similar biochemical modifications, such as the alteration of the protein pattern, the induction of oxidative stress mechanisms, and the deregulation of lipid and carbohydrate metabolisms. These evidences suggest that unilateral endometriosis impairs the overall ovarian functions, causing alterations not only in the ovary with endometriotic lesions but also in the contralateral "healthy" one.
_____

Key words: Unilateral Ovarian Endometriosis, FTIR microspectroscopy, Raman microspectroscopy,

Multivariate analysis

Introduction

Endometriosis is a chronic gynaecological disease characterised by the presence of epithelial, glandular and stromal endometrial cells in extra-uterine districts [1]. It is reported that 30% to 50% of women with a diagnosis of endometriosis are affected by infertility [2]. Several factors have been suggested as possible causes of endometriosis-associated infertility: pelvic adhesions, luteinized unruptured follicles, immunologic alterations, progesterone resistance, and impairment of folliculogenesis, ovulation, ovum transport, fertilization, and implantation [3–8]. The characteristics of this infertility are variable, and women affected by endometriosis can display a decrease of fertilization, implantation and pregnancy rates [9]. To avoid infertility problems, in women affected by unilateral ovarian endometriosis (UOE), oocytes are routinely collected in Assisted Reproductive Technology (ART) practice from the contralateral ovary, which does not show endometriotic lesions and hence can be considered healthy [10].

Several studies reported that the presence of endometriotic lesions can directly impair also the activity of Granulosa cells (GCs), somatic cells that surround the oocyte [11–13]. GCs are responsible for many important follicular functions, such as the production of oestradiol during follicular growth, the production of essential nutrients used as an energy source during oocyte maturation, the accumulation of oocyte secreted metabolites, and the secretion of progesterone after ovulation [14–17]. A dysregulation in these functions can lead to severe cellular damages, causing decreased rates of oocyte nuclear maturation and fertilization [18–20].

Fourier Transform InfraRed Microspectroscopy (FTIRM) and Raman MicroSpectroscopy (RMS) are powerful vibrational techniques, widely applied in life sciences for the study of the biomolecular building and composition of cells [21–23]. They present the advantage to be label-free, since each molecule has a proper IR and Raman spectrum. The analysis of IR and Raman bands in terms of position, intensity and width, makes possible to obtain a unique molecular fingerprint of the most relevant biological molecules (proteins, lipids, sugars and nucleic acids) inside the analysed samples [24–26]. This chemical information can be directly related to specific biological processes, such as cellular activity, metabolism and oxidative stress [27–29]. IR absorption and Raman spectroscopies can be considered to be mutually complementary due to the difference in physical origin of the processes. Whereas IR absorption is sensitive to polar (usually antisymmetric) group vibrations, Raman is sensitive to polarizable (usually symmetric) group vibrations. Thus, the combination of the techniques gives a more complete analysis of the complete biological specimen. In addition, in the

2

conventional microscopic forms, FTIR has a spatial resolution of ~10 μm, whereas with a x 100 objective, confocal Raman microscopic resolutions of <1 μm can be achieved. FTIR can have the advantage of averaging larger areas, while Raman microspectroscopy can enable subcellular analysis [30,31].

Recently, our team applied FTIRM for the vibrational characterization of both human oocytes and GCs [32,33]. Furthermore, preliminary FTIRM tests were also carried out on GCs collected from patients with diagnosis of unilateral ovarian endometriosis (UOE), and unexpected results were obtained, shedding new light on the effects of UOE on GC metabolism. In fact, the macromolecular profile of GCs collected from patients affected by this disease was very similar, irrespective of the ovary they were recovered from [34,35]. Pursuing this approach further, a multidisciplinary study, which applies the analytical spectroscopic methods of both FTIRM and RMS to the study of this gynecological disease, was performed, aiming to provide a more fundamental understanding of the biochemical modifications induced by unilateral ovarian endometriosis in the metabolism of GCs collected from the contralateral "healthy" ovary with respect to those from the ovary with endometriotic lesions.

Experimental section

The study, approved by the Ethics Committee of 9.Baby Center for Reproductive Health (Bologna, Italy), was carried out in full accordance with ethical principles for experiments involving humans, include The Code of Ethics of the World Medical Association (Declaration of Helsinki, 2013). To participate in this investigation, patients signed an informed consent, which included the donation of GCs. All samples were strictly anonymous, and it was impossible to correlate them to patients.

Luteinized GCs sample collection

N. 20 patients (N. 10 with diagnosis of unilateral ovarian endometriosis and N. 10 with diagnosis of tubal, idiopathic or male infertility) were enrolled in an *in vitro* fertilization program, according to the following inclusion criteria: 35±2.8 of age; non-smokers; regular ovulatory menstrual cycles; FSH<10 IU/I on day 3 of the menstrual cycle.

Controlled ovarian stimulation was induced using leuprorelin (Enantone, Takeda, Rome, Italy) and recombinant follicle-stimulating hormone (rFSH) (Gonal-F, Serono, Rome, Italy, or Puregon Organon, Rome, Italy). Human chorionic gonadotropin (HCG) at 10,000 IU

(Gonasi, Amsa, Rome, Italy) was administered when one or more follicles reached a diameter of *ca.* 23 mm [36]. At the end of the treatment, from each patient, a pool of luteinized GCs was collected from all the follicles, according to the following protocol. GCs undergo luteinisation after ovulation, at a specific moment of the ovarian cycle; since they are crucial for the development of the oocyte and for pregnancy, luteinized GCs are commonly used to study of ovarian functions [37]. Follicular fluid was centrifuged at 1100x g for 10 min and the pellet was resuspended in 2 mL of Sydney IVF Gamete Buffer Medium (Cook IVF, Brisbane, Australia), overlaid on 80%-40% discontinuous gradient of silica particles suspension (1 mL PureSperm 40 and 1 mL PureSperm 80; Nidacon, Goteborg, Sweden), and centrifuged at 1600x g for 13 min to separate GCs from red blood cells. After centrifugation, three layers were observed: a top layer containing the follicular fluid, a middle ring-like layer containing GCs and a bottom layer containing erythrocytes. GCs were recovered in the middle ring-like layer using a Pasteur pipette and placed into 1 mL of NaCl 0.9% solution (Fresenius Kabi). Isolated GCs were centrifuged at 300x g for 10 minutes. The supernatant was discarded, and the pellet re-suspended in 1 mL of NaCl 0.9% solution and washed again at 300x g for 10 minutes. After additional centrifugation for 5 min at 600x g, the cell pellet was re-suspended in 100 μl of sterile NaCl 0.9% solution.

GCs samples were divided into the following experimental groups: **CTRL** (N. 10 GCs samples collected from the ovaries of women with diagnosis of tubal, idiopathic or male infertility, taken as control group), **ENDO** (N. 10 GCs samples collected from the ovary with diagnosis of unilateral ovarian endometriosis), and **CONTRAL** (N. 10 GCs samples collected from the contralateral "healthy" ovary).

FTIRM measurements and data analysis

N. 5 aliquots of each GCs sample were deposited without any fixation process onto CaF_2 optical windows (1-mm thick, 13-mm diameter) and air-dried for 30 min, in order to avoid water contributions to the IR spectra [33]. FTIRM measurements were performed, within the same day of collection, at the infrared Beamline SISSI (Synchrotron Infrared Source for Spectroscopic and Imaging), Elettra Sincrotrone Trieste (Trieste, Italy). A Hyperion 3000 Vis-IR microscope equipped with a HgCdTe (MCT_A) detector and coupled with a Vertex 70 interferometer (Bruker Optics, Ettlingen, Germany) was used.

From each aliquot of GCs sample, ~10 areas containing densely packed cell monolayers were selected by visible microscopy, from which IR spectra were collected in transmission mode in the MIR region (4000 - 800 cm^{-1}) [33]. Knife-edge apertures were set at 30×30 μm^2

(512 scans, spectral resolution of 4 cm^{-1}, zero-filling factor of 2 in the spectral range 4000−800 cm^{-1}, scanner velocity of 40 kHz). Background spectra were collected using the same parameters on clean zones of the CaF$_2$ optical windows. All IR spectra of each aliquot of GCs sample were averaged (Averaging routine, OPUS 7.1 software) and then corrected for the contribution of atmospheric carbon dioxide and water vapour (Atmospheric compensation routine, OPUS 7.1 software). Average spectra (50 for each experimental group), obtained by this procedure, were evaluated in terms of S/N ratio on the basis of the height of the band centred at ~1660 cm^{-1} (Amide I band of proteins), which is always the highest peak of cell spectra; average spectra having at 1660 cm^{-1} an absorbance value lower than 0.07 a.u. (~20%) were discarded [28].

The remaining IR spectra were vector normalized, and then submitted to multivariate analyses, with no further pre-processing. The pairwise PCA analysis of **CTRL/ENDO**, **CTRL/CONTRAL** and **CONTRAL/ENDO** spectra was performed, by exploiting an in-house developed algorithm in R Studio (R Studio: Integrated Development for R. RStudio, Inc., Boston, MA). PCA was employed as an unsupervised multivariate approach to analyse spectral data of GCs. The order of the PCs denotes their importance to the dataset; PC1 describes the highest amount of variation [38]. The PC scores were also displayed by loading spectra, which contain peaks, both positive and negative that explain the spectral variation in the dataset; this tool is used as a method to separate spectra into groups.

For a more detailed analysis, for each experimental group the average absorbance spectrum, together with its standard deviation spectra (average absorbance spectra ± standard deviation spectra) were calculated (Averaging routine, OPUS 7.1 software). Average absorbance spectra ± standard deviation spectra were then curve fitted in the following spectral regions: 3050–2800 cm^{-1}, 1790–1480 cm^{-1} and 1350-900 cm^{-1}. A Gaussian algorithm (GRAMS/AI 7.02, Galactic Industries, Inc., Salem, NH) was adopted on IR spectra upon straight baseline correction and vector normalization. The number of underlying bands and their centre values (expressed as wavenumbers) were precisely identified by second derivative results, and the integrated areas were calculated. The wavenumber, together with the vibrational mode, the label and the biological meaning of all the underlying bands are reported in Table 1. The mean values of the integrated areas of selected underlying bands with biological meaning were determined. In addition, the sum of the mean values of integrated areas of all the underlying bands in the 1790–1600 cm^{-1} region (corresponding to the Amide I band of proteins, named AI) and that of all the underlying bands in the 1350-900 cm^{-1} spectral range (named TOT) were also calculated. These values were used to calculate the following band area ratios:

179 CH/CH3, CH2/CH3, C=O/AI, FOLDED/AI, UNFOLDED/AI, Ph1/TOT, RNA1/TOT,

180 Ph2/TOT, GLYCO/TOT, DNA1/TOT, RNA2/TOT, DNA2/TOT, and Z-DNA/TOT. For

181 labels and biological and vibrational meaning, see Table 1.

182

Table 1
IR vibrational modes highlighted by Peak Fitting procedure in **CTRL**, **CONTRAL** and **ENDO** absorbance average spectra. For each peak, the wavenumber, together with the vibrational mode, the label and the biological meaning are reported.

Range (cm^{-1})	Wavenumber (cm^{-1})	Vibrational mode	Label	Biological meaning
3050-2800	~3012	Stretching vibration of =CH groups	CH	Mainly lipid alkyl chains [32,56]
	~2957, ~2869	Asymmetric and symmetric stretching vibrations of CH$_3$ groups	CH3	
	~2925, ~2852	Asymmetric and symmetric stretching vibrations of CH$_2$ groups	CH2	
1790-1480	~1746	Stretching vibration of C=O ester moieties	C=O	Lipid peroxidation [42]
	~1694	Vibrational modes of β-turn secondary structures		Proteins secondary structure [57]
	~1680,~1627, ~1613	Vibrational modes of β-sheet secondary structures	FOLDED	
	~1659	Vibrational modes of α-helix secondary structures		
	~1640	Vibrational modes of random coil secondary structures	UNFOLDED	
1350-900	~1240	Asymmetric stretching vibration of PO$_2$- groups	Ph1	Mainly phosphorylated proteins [42,58]
	~1118	Stretching vibration of C-OH groups of ribose	RNA1	RNA [32,57,59]
	~994	Stretching vibration of uracil ring	RNA2	
	~1087	Symmetric stretching vibration of PO$_2$- groups	Ph2	Mainly phosphate backbone of nucleic acids [28]
	~1053	Stretching vibrations of C-O-C and C-OH groups of carbohydrates	GLYCO	Carbohydrates [28]
	~1020	Stretching vibration of C–O groups in DNA	DNA1	DNA [32,57,59]
	~970	Vibrational modes of DNA backbone	DNA2	
	~924	Left-handed helix DNA vibrations	Z-DNA	Z-DNA [32,60]

183

184 *RMS measurements and data analysis*

185

186 RMS measurements were carried out at the FOCAS Research Institute, Dublin (Ireland).

187 For Raman measurements, each GC samples were divided into N. 5 aliquots and fixed in a

188 4% paraformaldehyde (PFA) solution for 10 min, washed twice in physiological solution, and

then stored at 4°C until RMS measurements. This procedure has been demonstrated to retain the biochemical profile of the cell as close as possible to that of live cells [39], maintaining hydration, while preserving them from biological damage during shipping [24]. From each GCs aliquot 10 point spectra were acquired on cells seeded on the glass slide, targeting nuclei of the cells. No contribution of glass to the spectra was observed.

A Horiba Jobin-Yvon LabRAM HR800 spectrometer, equipped with a 532-nm diode laser (~50 mW laser power) as source was used. All measurements were acquired by using a x100 objective (Olympus, N.A. 1). The spectrometer was calibrated to the 520.7 cm^{-1} line of silicon prior to spectral acquisition. A 600 lines per mm grating was chosen. A 100 μm confocal pinhole was used for all measurements. The spectra were dispersed onto a 16-bit dynamic range Peltier cooled CCD detector. The spectral range from 1800 to 400 cm^{-1}, the so-called fingerprint region, was chosen and spectra were acquired for 3x10 seconds at each spot. For each GCs aliquot, the average RMS spectrum was calculated (Averaging routine, OPUS 7.1 software). Average spectra were smoothed using 7 smoothing points, baseline-corrected with the polynomial method (2 iterations) (OPUS 7.1 software), and then submitted to multivariate analysis. The pairwise PCA analysis of **CTRL/ENDO**, **CTRL/CONTRAL** and **CONTRAL/ENDO** spectra was performed, by exploiting an in-house developed algorithm in R Studio.

The wavenumber of the most relevant peaks found in Raman spectra, together with the vibrational mode, the label and the biological meaning are reported in Table 2. The height of such peaks was also calculated (Integration mode K, OPUS 7.1 software).

210

Table 2
Vibrational modes highlighted in the 1800-400 cm^{-1} spectral region of **CTRL**, **CONTRAL** and **ENDO** Raman average spectra. For each peak, the wavenumber, together with the vibrational mode, the label and the biological meaning are reported.

Wavenumber (cm^{-1})	Vibrational mode	Label	Biological meaning
~1657	Stretching vibration of amidic C=O groups	PROTEINS	Cellular proteins [61]
~1615	Stretching vibrations of tyrosine and tryptophan C=C groups	TYR-TRP	Tyrosine and Tryptophan amino acid residues [62]
~1605	Stretching vibrations of phenylalanine and tyrosine C=C groups	PHE-TYR	Phenylalanine and Tyrosine amino acid residues [63]
~1263	Amidic C-N stretching and N-H bending vibrations, mainly due to helix structures	HELIX	Helical secondary structures of proteins [62]
~1003	Symmetric stretching breathing vibration of phenylalanine	PHE	Phenylalanine amino acid residues [64]
~980	C-C stretching vibration of beta-sheets structures	BETA	Beta-sheets secondary structures of proteins [65]
~855	C-C stretching vibration of proline sidechains	PRO	Proline amino acid residues [63]
~642	C-C twisting vibration of tyrosine	TYR	Tyrosine amino acid residues [38]

211

212 *Statistical analysis*

213

214   Normally distributed data deriving from RMS and FTIRM spectra were presented as mean

215 ± S.D. Significant differences between experimental groups were determined by means of a

216 factorial analysis of variance (one-way ANOVA), followed by Tukey's multiple comparisons

217 test, using the statistical software package Prism6 (Graphpad Software, Inc. USA). One-way

218 ANOVA compares the means of **CTRL**, **CONTRAL** and **ENDO** groups in order to make

219 inferences about the population means. Statistical significance was set at $p<0.05$. Different

220 letters over box charts indicate statistically significant differences among the above defined

221 experimental groups.

222

223

224 **Results**

225

226   Luteinized GCs samples separately collected from both ovaries of women affected by UOE

227 (the ovary with endometriotic lesions, **ENDO**, and the contralateral "healthy" one,

228 **CONTRAL**) were analysed by FTIR and Raman microspectroscopy. The spectral data were

229   compared with those of GCs from women with diagnosis of tubal, idiopathic or male infertility

230   (taken as control group, **CTRL**).

231

232   *FTIRM analysis*

233

234   In Fig. 1, the pairwise PCA scatter plots of GCs IR spectra from **CTRL**/**CONTRAL**,

235   **CTRL**/**ENDO** and **CONTRAL**/**ENDO** groups and the relative loadings are reported. A

236   partial differentiation according to PC1 was detectable in **CTRL**/**CONTRAL** and

237   **CTRL**/**ENDO** scatter plots (respectively, 71.46% and 70.26% of explained system variance)

238   (Figs. 1A,B); conversely, no separation was detected between **CONTRAL** and **ENDO** groups

239   (Fig. 1C). The same discriminant spectral features were observed by the analysis of PC1

240   loadings of **CTRL**/**CONTRAL** and **CTRL**/**ENDO**. In particular, differences were observed

241   in the regions at 3050-2800 cm^{-1} (stretching modes of alkyl groups in lipids), 1790-1480 cm^{-1}

242   (vibrational modes of Amide I and II bands of proteins), and 1350-900 cm^{-1} (stretching

243   modes of phosphates and carbohydrates) (Figs. 1D,E). Conversely, no relevant discriminating

244   spectral features were observed in the **CONTRAL**/**ENDO** loading plot (Fig. 1F).

245
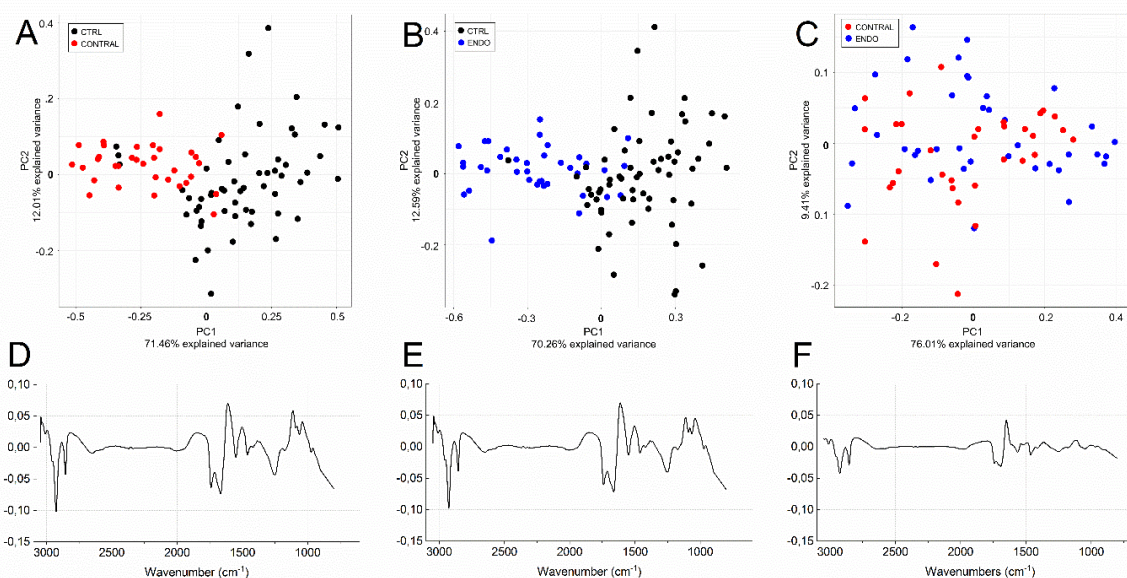
Fig. 1 Multivariate analysis of FTIRM data. Pair-wise PCA scatter plots calculated for **CTRL/CONTRAL** (A), **CTRL/ENDO** (B) and **CONTRAL/ENDO** (C) spectra. PC1 loadings of **CTRL/CONTRAL** (D), **CTRL/ENDO** (E), and **CONTRAL/ENDO** (F) experimental groups.

246

247   In Fig. 2, IR spectra of CTRL, CONTRAL and ENDO GCs in the 3100-2700 cm^{-1} (Fig.

248   2A) and 1800-800 cm^{-1} (Fig. 2B) regions are presented. As expected from the loadings

249   analysis, tiny changes were observed by comparing the spectral profile of GCs from the

different experimental groups, above all in the lipid region (3050-2800 cm^{-1}) as well as in the 1300 – 900 cm^{-1} range ascribable to phosphate groups and carbohydrates. Hence, for a more in-depth analysis, **CTRL**, **CONTRAL** and **ENDO** GCs spectra were curve fitted in the 3050–2800 cm^{-1}, 1790–1480 cm^{-1} and 1350-900 cm^{-1} spectral ranges and the integrated areas of the underlying bands were used to calculate specific band area ratios (see Experimental Section).
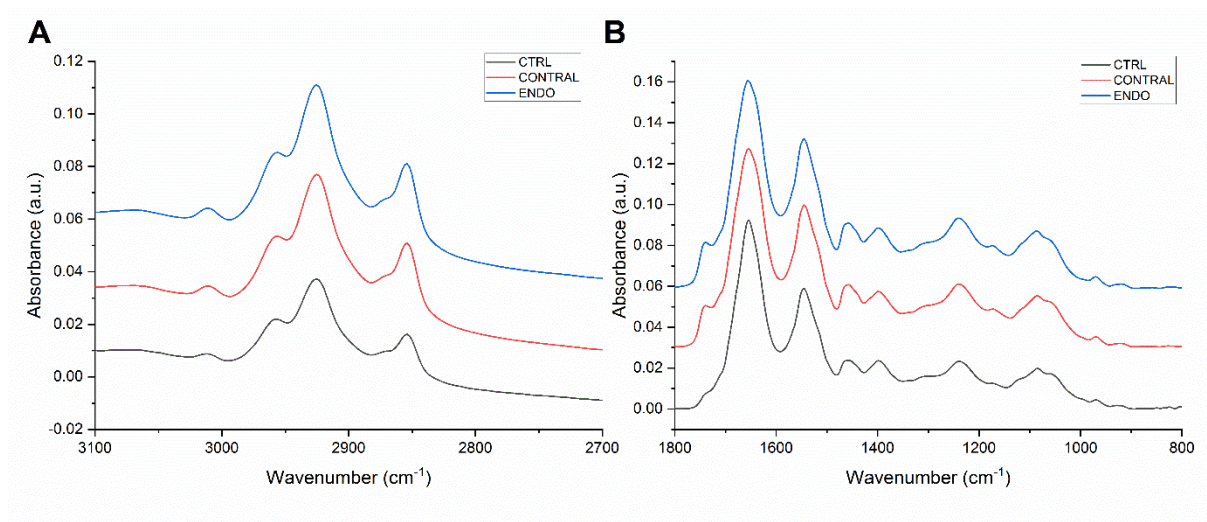

Fig. 2 IR spectra of **CTRL** (black line), **CONTRAL** (red line), and **ENDO** (blue line) GCs interpolated in the following spectral ranges: (A) 3100-2700 cm^{-1}; (B) 1800-800 cm^{-1}. For better viewing, spectra are shifted along y axis; absorbance is reported in arbitrary units (a.u.).

The statistical analysis of the numerical variations of these band area ratios is showed in Figs. 3 and 4. The following results have been achieved in both **CONTRAL** and **ENDO** GCs with respect to **CTRL** ones: (i) the ratio CH/CH3 (indicating the unsaturation degree of lipid alkyl chains) significantly increased (Fig. 3A); (ii) the ratio CH2/CH3 (indicating the saturation degree of lipid alkyl chains) significantly decreased (Fig. 3B); (iii) the ratio C=O/AI (indicating the amount of peroxidised lipids) significantly increased (Fig. 3C); (iv) the ratio FOLDED/AI (indicating the amount of properly folded proteins) significantly decreased (Fig. 3D); (v) the value UNFOLDED/AI (indicating the degree of unfolded structures in proteins) significantly increased (Fig. 3E); (vi) the ratio Ph1/TOT (indicating the amount of phosphate groups mainly in proteins) significantly increased (Fig. 4A); (vii) the ratios RNA1/TOT and RNA2/TOT (both indicating the amount of RNA) significantly decreased (Figs. 4B,F); (viii) the ratio Ph2/TOT (indicating the amount of phosphate groups in nucleic acids) did not significantly change (Fig. 4C); (ix) the ratio GLYCO/TOT (indicating the amount of carbohydrates) significantly decreased (Fig. 4D); (x) the ratios DNA1/TOT and DNA2/TOT (both indicating the amount of DNA) did not significantly change (Figs. 4E,G), and (xi) the ratio Z-DNA/TOT (indicating the amount of Z-DNA) significantly increased (Fig. 4H).
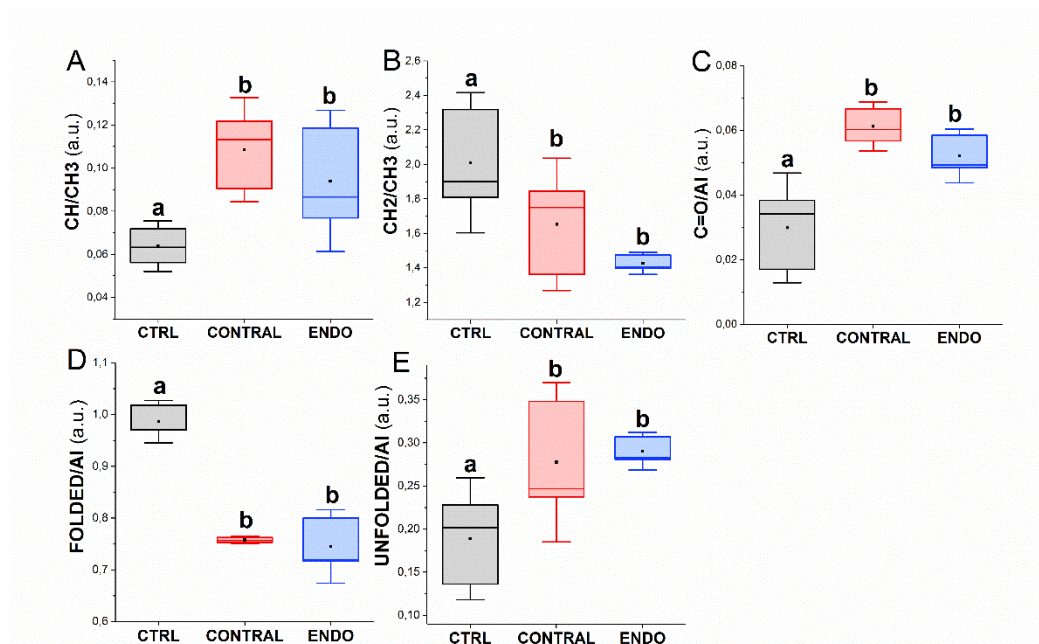
Fig. 3 Box charts showing the numerical variation of the following band area ratios calculated for **CTRL**, **CONTRAL** and **ENDO** GCs: (A) CH/CH3; (B) CH2/CH3; (C) C=O/AI; (D) FOLDED/AI; (E) UNFOLDED/AI. Centre line marks the median, edges indicate the 25th and the 75th percentile, whiskers indicate standard deviation, and the black square marks the mean. Different letters over box charts indicate statistically significant differences among groups (one-way ANOVA and Tukey's multiple comparisons test). Statistical significance was set at $p<0.05$.
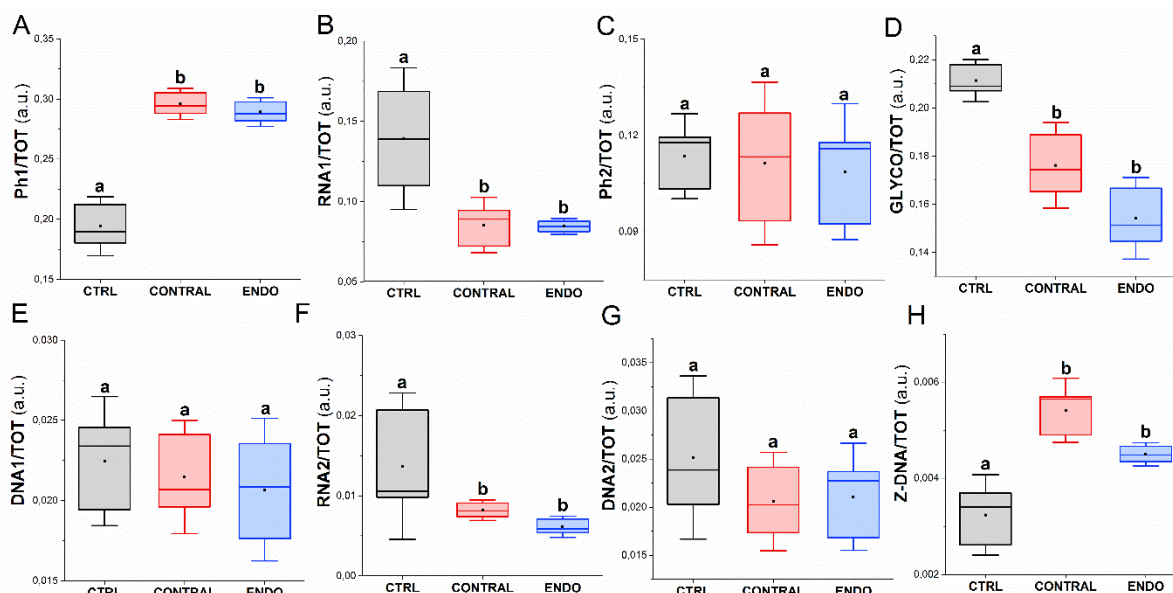
Fig. 4 Box charts showing the numerical variation of the following band area ratios calculated for **CTRL**, **CONTRAL** and **ENDO** GCs: (A) Ph1/TOT; (B) RNA1/TOT; (C) Ph2/TOT; (D) GLYCO/TOT; (E) DNA1/TOT; (F) RNA2/TOT; (G) DNA2/TOT; (H) Z-DNA/TOT. Centre line marks the median, edges indicate the 25th and the 75th percentile, whiskers indicate standard deviation, and the black square marks the mean. Different letters over box charts indicate statistically significant difference among groups (one-way ANOVA and Tukey's multiple comparisons test). Statistical significance was set at $p<0.05$.
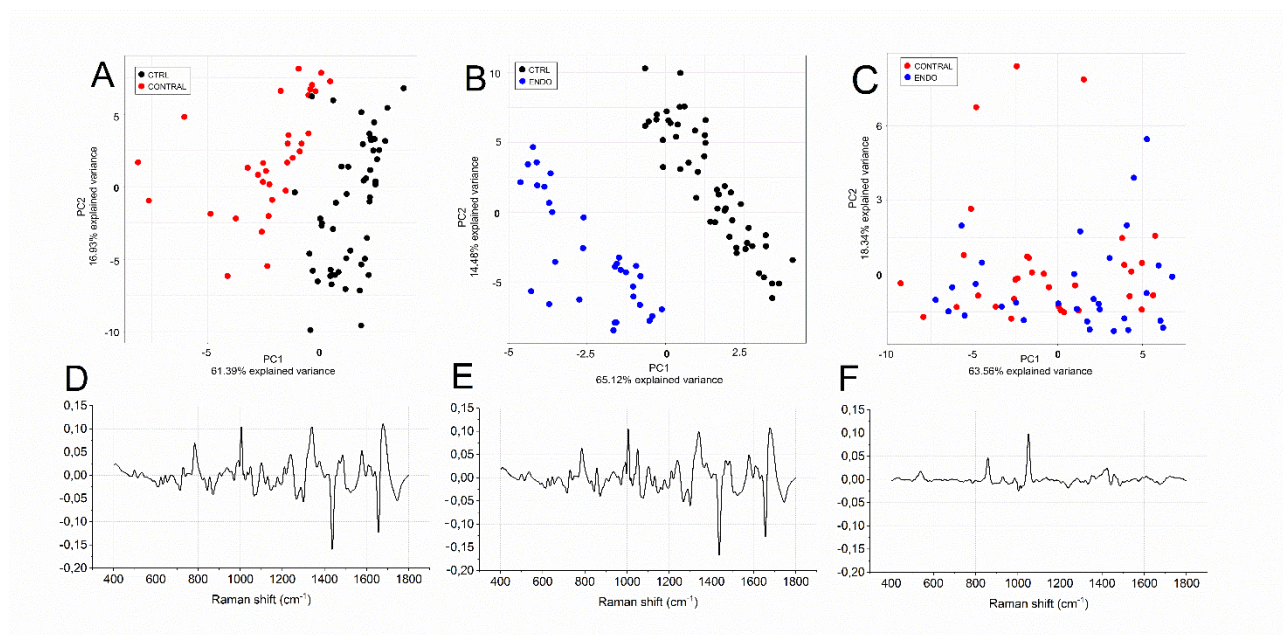
RMS analysis

275   In Fig. 5, the pairwise PCA scatter plots of GCs Raman spectra from **CTRL**/**CONTRAL**,

276 **CTRL/ENDO** and **CONTRAL/ENDO** groups and the relative loadings are reported. A clear

277 segregation was observed along PC1 axis both for **CTRL/CONTRAL** and **CTRL/ENDO**

278 spectra (61.39% and 65.12% of explained system variance, respectively) (Figs. 5A,B).

279 Conversely, no separation was detected in **CONTRAL/ENDO** plot (Fig. 5C), as confirmed

280 also by PC1 loading of **CONTRAL/ENDO** populations (Fig. 5F). Conversely, the PC1

281 loadings of **CTRL/CONTRAL** and **CTRL/ENDO** analyses showed relevant modifications

282 in the whole examined spectral range (1800-400 cm^{-1}) (Figs. 5D,E).

283

Fig. 5 Multivariate analysis of RMS data. Pair-wise PCA scatter plots calculated for **CTRL/CONTRAL** (A), **CTRL/ENDO** (B) and **CONTRAL/ENDO** (C) spectra. PC1 loadings of **CTRL/CONTRAL** (D), **CTRL/ENDO** (E), and **CONTRAL/ENDO** (F) experimental groups.

284

285   In Fig. 6, RMS spectra of **CTRL**, **CONTRAL** and **ENDO** GCs in the 1800-400 cm^{-1} range

286 are presented. As already identified by the analysis of loadings, changes in the spectral profile

287 of **CONTRAL** and **ENDO** GCs with respect to **CTRL** ones were observed above all in the

288 band centered at ~1660 cm^{-1}, assigned to proteins, and also in the bands associated with

289 protein secondary structures (~1263 and ~980 cm^{-1}, attributable respectively to helical and

290 beta structures) and aromatic amino acids (~1615, ~1605, ~1003 and ~642 cm^{-1},

291 corresponding to phenylalanine, tyrosine, and tryptophan).
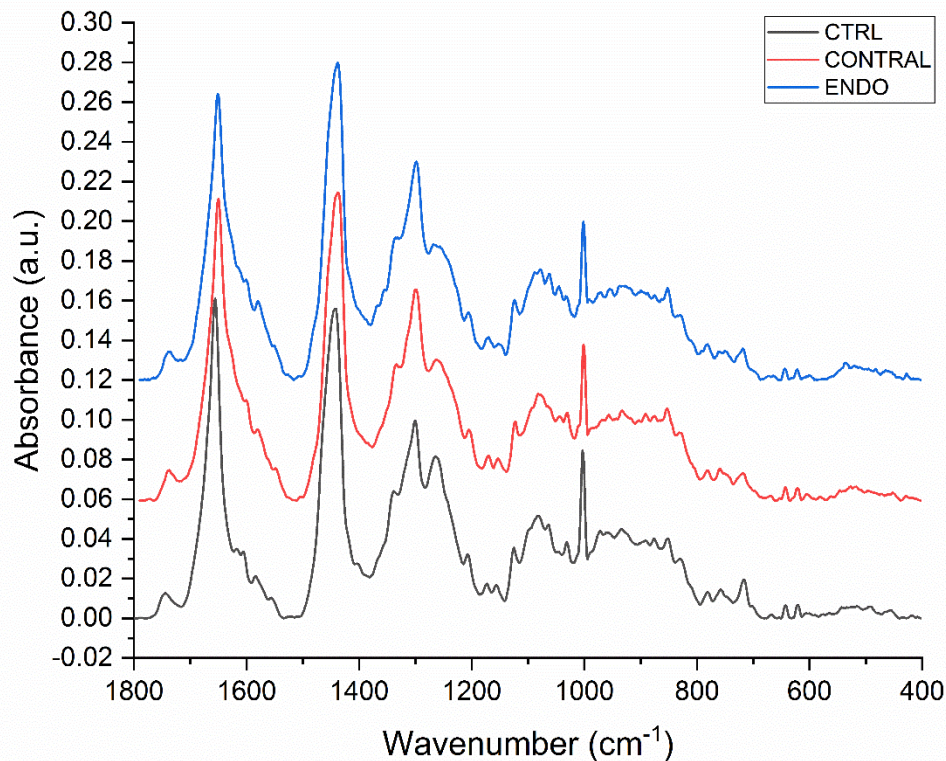
Fig. 6 RMS spectra of **CTRL** (black line), **CONTRAL** (red line), and **ENDO** (blue line) GCs interpolated in the 1800-400 cm^{-1} range. For better viewing, spectra are shifted along y axis; absorbance is reported in arbitrary units (a.u.).

The statistical analysis of the numerical variations of heights of the peaks, reported in Table 2, is shown in Fig. 7. The following results have been achieved in both **CONTRAL** and **ENDO** GCs with respect to **CTRL** ones: (i) the height of PROTEINS (indicating the total amount of cellular proteins) showed a significant decrease (Fig. 7A); (ii) the height of HELIX (indicating the amount of helical secondary structures of proteins) showed a significant decrease (Fig. 7B); (iii) the height of BETA (indicating the amount of β-sheet secondary structures of proteins) showed a significant decrease (Fig. 7C); (iv) the height of TYR-TRP (indicating the amount of tyrosine and tryptophan amino acids) showed a significant decrease (Fig. 7D); (v) the height of PHE-TYR (indicating the amount of phenylalanine and tyrosine amino acids) significantly decreased (Fig. 7E); (vi) the height of PHE (indicating the amount of phenylalanine amino acid) significantly decreased (Fig. 7F); (vii) the height of PRO

13

326 (indicating the amount of proline amino acid) significantly increased (Fig. 7G); (viii) the

327 height of TYR (indicating the amount of tyrosine amino acid) significantly decreased (Fig.

328 7H). All the other bands highlighted as different by the PC1 loading were investigated but did

329 not show significant alterations among the experimental groups (data not shown).

330
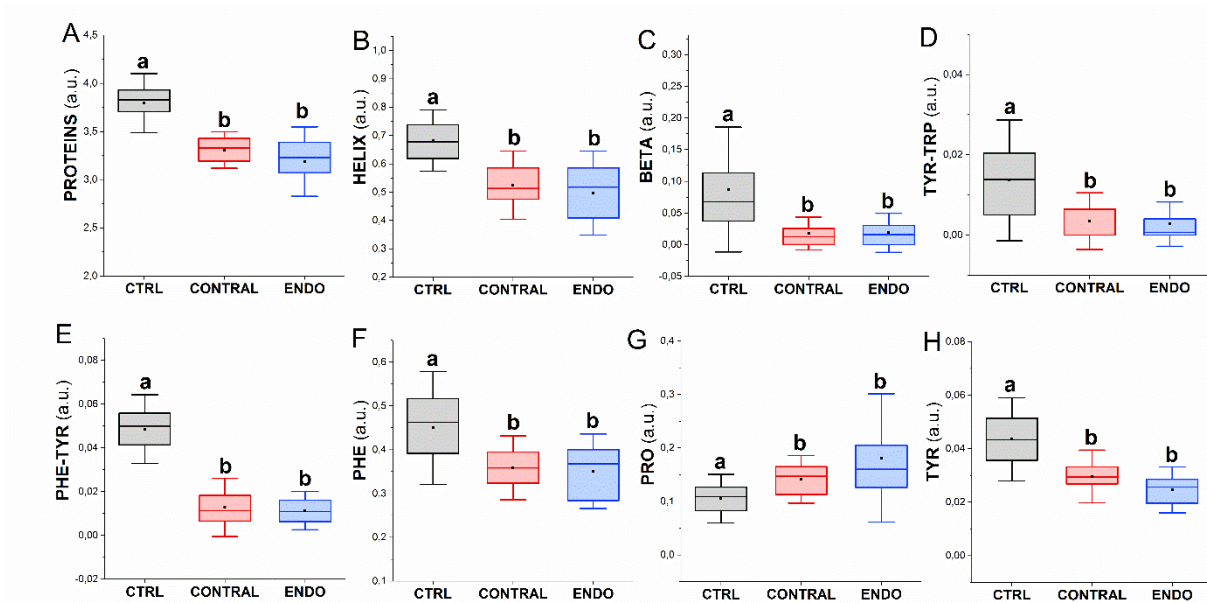
Fig. 7 Box charts showing the variation of height values of the following bands calculated for **CTRL**, **CONTRAL** and **ENDO** GCs: (A) PROTEINS; (B) HELIX; (C) BETA; (D) TYR-TRP; (E) PHE-TYR; (F) PHE; (G) PRO, and (H) TYR. Centre line marks the median, edges indicate the 25th and the 75th percentile, whiskers indicate standard deviation, and the black square marks the mean. Different letters above box charts indicate statistically significant difference among groups (one-way ANOVA and Tukey's multiple comparisons test). Statistical significance was set at $p<0.05$.

331

332

Discussion

334

335　　FTIRM and RMS techniques are currently applied in the biomedical field, due to the

336 possibility to obtain, at the same time, in a label-free way and on the same sample, a unique

337 molecular fingerprint of the most relevant biological molecules. In this study, a vibrational

338 approach has been performed to profoundly investigate the effects of UOE on the biochemical

339 composition and metabolism of GCs collected from the ovary with endometriotic lesions, and

340 the contralateral "healthy" one.

341   Endometriosis is known to be related to an impairment of folliculogenesis [6]. Given the

342 importance of GCs on follicle development, a dysregulation of their functions can lead to

343 severe damages to the oocyte [14,40,41].

344   It should be noted that, while the tightly focused laser spot for the RMS measurements

345 sampled only the nucleus, the lower resolution FTIRM measurements sampled typically 3-4

346 whole cells, including cytoplasm and nucleus. Nevertheless, individually and in combination,

347 the analysis of FTIRM and RMS data revealed, in both the ovaries of women with a diagnosis

348 of UOE, several layers of GCs impairment. In particular, the occurrence of lipid peroxidation

349 in **CONTRAL** and **ENDO** GCs with respect to **CTRL** ones was evidenced by the significant

350 increase of =CH groups (CH/CH3) and C=O ester moieties (C=O/AI), together with the

351 decrease of CH_2 groups (CH2/CH3) [42–45].

352   It is known that cellular oxidation targets not only lipids, but also proteins, leading to their

353 misfolding and creating internal cell stressors [46]. In fact, in both **CONTRAL** and **ENDO**

354 GCs, a significant impairment in proteins secondary structure was highlighted (decrease of

355 FOLDED/AI and HELIX and BETA, and increase of UNFOLDED/AI), together with the

356 decrease of tyrosine, tryptophan and phenylalanine amino acids (TYR, PHE, TYR-TRP and

357 PHE-TYR). All these findings suggested the attack of reactive oxygen species (ROS) to

358 proteins in general, and, in particular, to the aromatic amino acid side chains [47].

359   This oxidation picture is consistent with the well-known reduced follicular antioxidant

360 ability in women with diagnosis of endometriosis [48] and with the role played by oxidative

361 stress and ROS in the progression of the disease [49,50]. Hence, the occurrence in GCs from

362 both ovaries, of these alterations let hypothesize that oxidative processes triggered by

363 endometriotic lesions act not only locally, but also in a systemic way.

364   In addition, for the first time, the impairment in the carbohydrate metabolism of GCs caused

365 by UOE was observed (decreased value of GLYCO/TOT **in CONTRAL** and **ENDO** GCs).

366 Considering that glucose is fundamental for mammalian oocytes, and that it cannot be utilized

367 unless previously transformed into pyruvate by GCs, this alteration, caused by UOE, may be

368 considered crucial for oocytes functionality [51].

369   In this study, the occurrence of epigenetic effects caused by endometriosis on GCs, already

370 reported in literature, was confirmed (increased value of Z-DNA/TOT and decreased value of

371 RNA1/TOT and RNA2/TOT) [52,53]. Z-DNA is an elongated left-handed conformation of

372 DNA, which can be found in segments with specialized sequences, characterized by

373 alternations of purines and pyrimidines, especially alternating deoxycytidine and

374 deoxyguanosine residues [54]. Z-DNA spatial conformation is thought to be able to influence

375 transcriptional activity by excluding transcription factors [55]. This epigenetic effect was also

376 observed for the first time in GCs from contralateral ovary, confirming the systemic effects

377 of UOE.

378

379 **Conclusions**

380 In this context, the present vibrational study sheds new light on the alterations induced by

381 UOE on the metabolic status and biochemical composition of Granulosa Cells retrieved from

382 the ovary with endometriotic lesions; moreover, it highlights that the same impairment also

383 characterizes Granulosa Cells collected from the contralateral ovary, usually considered

384 "healthy". In fact, in GCs from both the ovaries of women affected by UOE, a similarly

385 profound alteration in the protein pattern was found, together with the same activation of

386 oxidative stress mechanisms, the dysregulation of carbohydrate metabolism, and the

387 modification in DNA methylation. Hence, these results open a new scenario, suggesting that

388 unilateral ovarian endometriosis acts not only locally, but also in a systemic way, causing

389 changes in the metabolic and macromolecular composition of GCs of both ovaries. Due to the

390 close relationship between Granulosa Cells and their companion oocyte, we suppose that UOE

391 likely causes an impairment in the whole ovarian functionality.

392 These findings could improve the knowledge on the infertility often observed in women

393 affected by UOE. In fact, in ART practice, oocytes are routinely collected from the

394 contralateral ovary, which does not show endometriotic lesions and hence is be considered

395 healthy. In contrast, our results suggest that the quality of oocytes retrieved from the

396 contralateral "healthy" ovary may be impaired in the same manner as those retrieved from the

397 affected ovary, suggesting the need to significantly revise the existing ART protocols.

398

399

400 **Conflicts of interest**

401 There are no conflicts to declare.

402

406

407 **References**

408 [1]   G. Benagiano, I. Brosens, D. Lippi, The history of endometriosis, Gynecol. Obstet. Invest. 78

16

409 (2014) 1–9. doi:10.1159/000358919.

[2] R. Checa, MA; Gonzalez-Comadran, M; Agramunt, S; Carreras, Fertility and Endometriosis, Clin. Obstet. Gynecol. 60 (2017) 497–502. doi:10.1097/GRF.0000000000000295.

[3] T. Tanbo, P. Fedorcsak, Endometriosis-associated infertility: aspects of pathophysiological mechanisms and treatment options, Acta Obstet. Gynecol. Scand. 96 (2017) 659–667. doi:10.1111/aogs.13082.

[4] J.A.W. Stilley, J.A. Birt, K.L. Sharpe-Timms, Cellular and molecular basis for endometriosis-associated infertility, Cell Tissue Res. 349 (2012) 849–862. doi:10.1007/s00441-011-1309-0.

[5] L.C. Giudice, L.C. Kao, Endometriosis, Lancet. 364 (2004) 1789–1799. doi:10.1016/S0140-6736(04)17403-5.

[6] A.M. Sanchez, V.S. Vanni, L. Bartiromo, E. Papaleo, E. Zilberberg, M. Candiani, R. Orvieto, P. Viganò, Is the oocyte quality affected by endometriosis? A review of the literature, J. Ovarian Res. 10 (2017). doi:10.1186/s13048-017-0341-4.

[7] D. de Ziegler, B. Borghese, C. Chapron, Endometriosis and infertility: pathophysiology and management, Lancet. 376 (2010) 730–738. doi:10.1016/S0140-6736(10)60490-4.

[8] B. Xu, N. Guo, X.-M. Zhang, W. Shi, X.-H. Tong, F. Iqbal, Y.-S. Liu, Oocyte quality is decreased in women with minimal or mild endometriosis, Sci. Rep. 5 (2015) 10779. doi:10.1038/srep10779.

[9] S. Kennedy, A. Bergqvist, C. Chapron, T. D 'hooghe, G. Dunselman, R. Greb, L. Hummelshoj, A. Prentice, E. Saridogan, ESHRE guideline for the diagnosis and treatment of endometriosis, Hum. Reprod. 20 (2005) 2698–2704. doi:10.1093/humrep/dei135.

[10] U. Leone, R. Maggiore, J.K. Gupta, S. Ferrero, Treatment of endometrioma for improving fertility, Eur. J. Obstet. Gynecol. 209 (2017) 81–85. doi:10.1016/j.ejogrb.2016.02.035.

[11] A.M. Sanchez, E. Somigliana, P. Vercellini, L. Pagliardini, M. Candiani, P. Vigano, Endometriosis as a detrimental condition for granulosa cell steroidogenesis and development: From molecular alterations to clinical impact, J. Steroid Biochem. Mol. Biol. 155 (2016) 35–46. doi:10.1016/j.jsbmb.2015.07.023.

[12] M. Toya, H. Saito, N. Ohta, T. Saito, T. Kaneko, M. Hiroi, Moderate and severe endometriosis is associated with alterations in the cell cycle of granulosa cells in patients undergoing in vitro fertilization and embryo transfer, Fertil. Steril. 73 (2000) 344–350.

[13] B. Wiweko, N. Muna, D.P. Gunawarti, R.U. Nasution, A. Zesario, High bax-bcl-2 Ratio Expression on Granulosa Cells from Endometriosis Patients, Adv. Sci. Lett. 23 (2017) 6720–6722. doi:10.1166/asl.2017.9380.

17

443 [14] E. Chronowska, High-Throughput Analysis of Ovarian Granulosa Cell Transcriptome,
444   Biomed Res. Int. 2014 (2014) 1–7. doi:10.1155/2014/213570.

445 [15] R.B. Gilchrist, M. Lane, J.G. Thompson, Oocyte-secreted factors: Regulators of cumulus cell
446   function and oocyte quality, Hum. Reprod. Update. 14 (2008) 159–177.
447   doi:10.1093/humupd/dmm040.

448 [16] D.A. Dumesic, D.R. Meldrum, M.G. Katz-Jaffe, R.L. Krisher, W.B. Schoolcraft, Oocyte
449   environment: Follicular fluid and cumulus cells are critical for oocyte health, Fertil. Steril.
450   103 (2015) 303–316. doi:10.1016/j.fertnstert.2014.11.015.

451 [17] R. Li, D.F. Albertini, The road to maturation: somatic cell interaction and self-organization
452   of the mammalian oocyte, Nat. Rev. Mol. Cell Biol. 14 (2013) 141–152.
453   doi:10.1038/nrm3531.

454 [18] S.M. Downs, J.L. Mosey, J. Klinger, Fatty acid oxidation and meiotic resumption in mouse
455   oocytes, Mol. Reprod. Dev. 76 (2009) 844–853. doi:10.1002/mrd.21047.

456 [19] L.L.-Y. Wu, K.R. Dunning, X. Yang, D.L. Russell, M. Lane, R.J. Norman, R.L. Robker,
457   High-Fat Diet Causes Lipotoxicity Responses in Cumulus–Oocyte Complexes and Decreased
458   Fertilization Rates, Endocrinology. 151 (2010) 5438–5445. doi:10.1210/en.2010-0551.

459 [20] X. Yang, L.L. Wu, L.R. Chura, X. Liang, M. Lane, R.J. Norman, R.L. Robker, Exposure to
460   lipid-rich follicular fluid is associated with endoplasmic reticulum stress and impaired oocyte
461   maturation in cumulus-oocyte complexes, Fertil. Steril. 97 (2012) 1438–1443.
462   doi:10.1016/j.fertnstert.2012.02.034.

463 [21] C. Matthäus, B. Bird, M. Miljković, T. Chernenko, M. Romeo, Infrared and Raman
464   Microscopy in Cell Biology, Methods Cell Biol. 89 (2008) 275–308. doi:10.1016/S0091-
465   679X(08)00610-9.Infrared.

466 [22] E. Giorgini, G. Gioacchini, S. Sabbatini, C. Conti, L. Vaccari, A. Borini, O. Carnevali, G.
467   Tosi, Vibrational characterization of female gametes: a comparative study., Analyst. 139
468   (2014) 5049–60. doi:10.1039/c4an00684d.

469 [23] F. Lyng, I. Ramos, O. Ibrahim, H. Byrne, Vibrational Microspectroscopy for Cancer
470   Screening, Appl. Sci. 5 (2015) 23–35. doi:10.3390/app5010023.

471 [24] M.J. Baker, J. Trevisan, P. Bassan, R. Bhargava, H.J. Butler, K.M. Dorling, P.R. Fielden,
472   S.W. Fogarty, N.J. Fullwood, K.A. Heys, C. Hughes, P. Lasch, P.L. Martin-Hirsch, B.
473   Obinaju, G.D. Sockalingum, J. Sulé-Suso, R.J. Strong, M.J. Walsh, B.R. Wood, P. Gardner,
474   F.L. Martin, Using Fourier transform IR spectroscopy to analyze biological materials, Nat.
475   Protoc. 9 (2014) 1771–1791. doi:10.1038/nprot.2014.110.

476 [25] W.F. Wolkers, H. Oldenhof, In situ FTIR studies on mammalian cells, Spectroscopy. 24

477   (2010) 525–534. doi:10.3233/SPE-2010-0474.

478   [26]   J.R. Baena, B. Lendl, Raman spectroscopy in chemical bioanalysis, Curr. Opin. Chem. Biol.

479   8 (2004) 534–539. doi:10.1016/j.cbpa.2004.08.014.

480   [27]   A. Downes, A. Elfick, Raman spectroscopy and related techniques in biomedicine, Sensors.

481   10 (2010) 1871–1889. doi:10.3390/s100301871.

482   [28]   E. Giorgini, S. Sabbatini, R. Rocchetti, V. Notarstefano, C. Rubini, C. Conti, G. Orilisi, E.

483   Mitri, D.E. Bedolla, L. Vaccari, In vitro FTIR microspectroscopy analysis of primary oral

484   squamous carcinoma cells treated with cisplatin and 5-fluorouracil: a new spectroscopic

485   approach for studying the drug–cell interaction, Analyst. (2018). doi:10.1039/C8AN00602D.

486   [29]   E. Giorgini, C. Conti, P. Ferraris, S. Sabbatini, G. Tosi, C. Rubini, L. Vaccari, G. Gioacchini,

487   O. Carnevali, Effects of Lactobacillus rhamnosus on zebrafish oocyte maturation: An FTIR

488   imaging and biochemical analysis, Anal. Bioanal. Chem. 398 (2010) 3063–3072.

489   doi:10.1007/s00216-010-4234-2.

490   [30]   H. Byrne, G.D. Sockalingum, N. Stone, Raman Microscopy : Complement or Competitor?,

491   in: Biomed. Appl. Synchrotron Infrared Microspectrosc. A Pract. Approach, RSC Analytical

492   Spectroscopy Monographs, 2011: pp. 105–142. doi:10.1039/9781849731997-00105.

493   [31]   F. Bonnier, A.D. Meade, S. Merzha, P. Knief, K. Bhattacharya, F.M. Lyng, H.J. Byrne,

494   Three dimensional collagen gels as a cell culture matrix for the study of live cells by Raman

495   spectroscopy, Analyst. 135 (2010) 1697. doi:10.1039/c0an00060d.

496   [32]   G. Gioacchini, E. Giorgini, L. Vaccari, P. Ferraris, S. Sabbatini, V. Bianchi, A. Borini, O.

497   Carnevali, A new approach to evaluate aging effects on human oocytes: Fourier transform

498   infrared imaging spectroscopy study, Fertil. Steril. 101 (2014) 120–127.

499   doi:10.1016/j.fertnstert.2013.09.012.

500   [33]   G. Gioacchini, V. Notarstefano, E. Sereni, C. Zacà, G. Coticchio, E. Giorgini, L. Vaccari, O.

501   Carnevali, A. Borini, Does the molecular and metabolic profile of human granulosa cells

502   correlate with oocyte fate? New insights by Fourier transform infrared microspectroscopy

503   analysis, MHR Basic Sci. Reprod. Med. (2018) 1–12. doi:10.1093/molehr/gay035.

504   [34]   G. Gioacchini, E. Sereni, C. Zacà, E. Giorgini, V. Notarstefano, L. Vaccari, O. Carnevali, A.

505   Borini, Could the unilateral ovarian endometriosis affect the contralateral ovary? New

506   insights from Fourier Transform Infrared (FTIR) spectroscopy, Fertil. Steril. 104 (2015)

507   e158.

508   [35]   G. Gioacchini, E. Sereni, C. Zacà, V. Notarstefano, L. Vaccari, E. Giorgini, A. Borini,

509   Fourier Transform Infrared (FTIR) spectroscopy as a new tool to assess molecular changes of

510   human granulosa cells induced by endometriosis, Hum. Reprod. 30 (2015) i276.

19

511 [36] A. Borini, R. Sciajno, V. Bianchi, E. Sereni, C. Flamigni, G. Coticchio, Clinical outcome of
512   oocyte cryopreservation after slow cooling with a protocol utilizing a high sucrose
513   concentration, Hum. Reprod. 21 (2005) 512–517. doi:10.1093/humrep/dei346.

514 [37] H. Ferrero, F. Delgado-Rosas, C.M. Garcia-Pascual, M. Monterde, R.C. Zimmermann, C.
515   Simon, A. Pellicer, R. Gomez, Efficiency and purity provided by the existing methods for the
516   isolation of luteinized granulosa cells: a comparative study, Hum. Reprod. 27 (2012) 1781–
517   1789. doi:10.1093/humrep/des096.

518 [38] Z. Farhane, H. Nawaz, F. Bonnier, H.J. Byrne, In vitro label-free screening of
519   chemotherapeutic drugs using Raman microspectroscopy: Towards a new paradigm of
520   spectralomics, J. Biophotonics. 11 (2018) e201700258. doi:10.1002/jbio.201700258.

521 [39] A.D. Meade, C. Clarke, F. Draux, G.D. Sockalingum, M. Manfait, F.M. Lyng, H.J. Byrne,
522   Studies of chemical fixation effects in human cell lines using Raman microspectroscopy,
523   Anal. Bioanal. Chem. 396 (2010) 1781–1791. doi:10.1007/s00216-009-3411-7.

524 [40] R.J. Kordus, H.A. LaVoie, Granulosa cell biomarkers to predict pregnancy in ART: pieces to
525   solve the puzzle, Reproduction. 153 (2017) R69–R83. doi:10.1530/REP-16-0500.

526 [41] T.B. Papler, E.V. Bokal, A. Maver, A.N. Kopitar, L. Lovrečić, Transcriptomic analysis and
527   meta-analysis of human granulosa and cumulus cells, PLoS One. 10 (2015) 1–22.
528   doi:10.1371/journal.pone.0136473.

529 [42] B. Vileno, S. Jeney, A. Sienkiewicz, P.R. Marcoux, L.M. Miller, L. Forró, Evidence of lipid
530   peroxidation and protein phosphorylation in cells upon oxidative stress photo-generated by
531   fullerols, Biophys. Chem. 152 (2010) 164–169. doi:10.1016/j.bpc.2010.09.004.

532 [43] A. Oleszko, S. Olsztyńska-Janus, T. Walski, K. Grzeszczuk-Kuć, J. Bujok, K. Gałecka, A.
533   Czerski, W. Witkiewicz, M. Komorowska, Application of FTIR-ATR spectroscopy to
534   determine the extent of lipid peroxidation in plasma during haemodialysis, Biomed Res. Int.
535   2015 (2015) 1–8. doi:10.1155/2015/245607.

536 [44] N. Benseny-Cases, O. Klementieva, M. Cotte, I. Ferrer, J. Cladera, Microspectroscopy
537   (μFTIR) reveals co-localization of lipid oxidation and amyloid plaques in human Alzheimer
538   disease brains, Anal. Chem. 86 (2014) 12047–12054. doi:10.1021/ac502667b.

539 [45] A. Rodríguez-Casado, I. Alvarez, A. Toledano, E. de Miguel, P. Carmona, Amphetamine
540   effects on brain protein structure and oxidative stress as revealed by FTIR
541   microspectroscopy, Biopolymers. 86 (2007) 437–446. doi:10.1002/bip.20753.

542 [46] N. Gregersen, P. Bross, S. Vang, J.H. Christensen, Protein Misfolding and Human Disease,
543   Annu. Rev. Genomics Hum. Genet. 7 (2006) 103–124.
544   doi:10.1146/annurev.genom.7.080505.115737.

545 [47] B.S. Berlett, E.R. Stadtman, Protein Oxidation in Aging, Disease, and Oxidative Stress, J.
546 Biol. Chem. 272 (1997) 20313–20316.

547 [48] L. Prieto, J.F. Quesada, O. Cambero, A. Pacheco, A. Pellicer, R. Codoceo, J.A. Garcia-
548 Velasco, Analysis of follicular fluid and serum markers of oxidative stress in women with
549 infertility related to endometriosis, Fertil. Steril. 98 (2012) 126–130.
550 doi:10.1016/j.fertnstert.2012.03.052.

551 [49] L.F.P. Carvalho, M.S. Abrão, C. Biscotti, R. Sharma, B. Nutter, T. Falcone, Oxidative Cell
552 Injury as a Predictor of Endometriosis Progression, Reprod. Sci. 20 (2013) 688–698.
553 doi:10.1177/1933719112466301.

554 [50] C. Ngô, C. Ché, C. Nicco, B. Weill, C. Chapron, F. Dé, R. Batteux, Reactive Oxygen Species
555 Controls Endometriosis Progression, Am. J. Pathol. 175 (2009) 225–234.

556 [51] M.L. Sutton-Mcdowall, R.B. Gilchrist, J.G. Thompson, The pivotal role of glucose
557 metabolism in determining oocyte developmental competence., Reproduction. 139 (2010)
558 685–95. doi:10.1530/REP-09-0345.

559 [52] M. Hayashi, Y. Yamashita, A. Hayashi, Y. Yoshida, S. Kawabe, M. Hayashi, Y. Terai, H.
560 Kamegai, M. Ohmichi, Expression and epigenetic change of the AR and FSHR genes in the
561 granulosa cells of endometriosis patients, Genet. Epigenetics. 1 (2012) 1–8.
562 doi:10.4137/GEG.S9877.

563 [53] E. Hosseini, F. Mehraein, M. Shahhoseini, L. Karimian, F. Nikmard, M. Ashrafi, P.
564 Afsharian, R. Aflatoonian, Epigenetic alterations of CYP19A1 gene in Cumulus cells and its
565 relevance to infertility in endometriosis, J. Assist. Reprod. Genet. 33 (2016) 1105–1113.
566 doi:10.1007/s10815-016-0727-z.

567 [54] A. Herbert, A. Rich, The biology of left-handed Z-DNA, J. Biol. Chem. 271 (1996) 11595–
568 11598. doi:10.1074/jbc.271.20.11595.

569 [55] S. Rothenburg, F. Koch-Nolte, F. Haag, DNA methylation and Z-DNA formation as
570 mediators of quantitative differences in the expression of alleles, Immunol. Rev. 184 (2001)
571 286–298. doi:10.1034/j.1600-065x.2001.1840125.x.

572 [56] C. Petibois, G. Déléris, Chemical mapping of tumor progression by FT-IR imaging: towards
573 molecular histopathology, Trends Biotechnol. 24 (2006) 455–462.
574 doi:10.1016/j.tibtech.2006.08.005.

575 [57] E. Giorgini, S. Sabbatini, C. Conti, C. Rubini, R. Rocchetti, M. Re, L. Vaccari, E. Mitri, V.
576 Librando, Vibrational mapping of sinonasal lesions by Fourier transform infrared imaging
577 spectroscopy., J. Biomed. Opt. 20 (2015) 125003. doi:10.1117/1.JBO.20.12.125003.

578 [58] P.T.T. Wong, R.K. Wong, T.A. Caputo, T.A. Godwin, B. Rigas, Infrared spectroscopy of

579   exfoliated human cervical cells : Evidence of extensive structural changes during

580   carcinogenesis, Proc. Natl. Acad. Sci. 88 (1991) 10988–10992.

581   [59]   B.R. Wood, B. Tait, D. McNaughton, Fourier Transform Infrared Spectroscopy as a Method

582   for Monitoring the Molecular Dynamics of Lymphocyte Activation, Appl. Spectrosc. 54

583   (2000) 353–359. doi:10.1366/0003702001949627.

584   [60]   G.I. Dovbeshko, V.I. Chegel, N.Y. Gridina, O.P. Repnytska, Y.M. Shirshov, V.P. Tryndiak,

585   I.M. Todor, G.I. Solyanik, Surface enhanced IR absorption of nucleic acids from tumor cells:

586   FTIR reflectance study, Biopolymers. 67 (2002) 470–486. doi:10.1002/bip.10165.

587   [61]   E. Efeoglu, M.A. Maher, A. Casey, H.J. Byrne, Toxicological assessment of nanomaterials:

588   the role of in vitro Raman microspectroscopic analysis, Anal. Bioanal. Chem. 410 (2018)

589   1631–1646. doi:10.1007/s00216-017-0812-x.

590   [62]   A. Rygula, K. Majzner, K.M. Marzec, A. Kaczor, M. Pilarczyk, M. Baranska, Raman

591   spectroscopy of proteins: a review, J. Raman Spectrosc. 44 (2013) 1061–1076.

592   doi:10.1002/jrs.4335.

593   [63]   I.R. Ramos, A.D. Meade, O. Ibrahim, H.J. Byrne, M. McMenamin, M. McKenna, A. Malkin,

594   F.M. Lyng, Raman spectroscopy for cytopathology of exfoliated cervical cells, Faraday

595   Discuss. 187 (2016) 187–198. doi:10.1039/C5FD00197H.

596   [64]   E. Efeoglu, A. Casey, H.J. Byrne, In vitro monitoring of time and dose dependent

597   cytotoxicity of aminated nanoparticles using Raman spectroscopy, Analyst. 141 (2016)

598   5417–5431. doi:10.1039/C6AN01199C.

599   [65]   Z. Movasaghi, S. Rehman, I.U. Rehman, Raman Spectroscopy of Biological Tissues, Appl.

600   Spectrosc. Rev. 42 (2007) 493–541. doi:10.1080/05704928.2014.923902.

601